TU Delft

Delft University of Technology

Document Version
Final published version

Licence
CC BY

Citation (APA)
Khokhar, M., Norder, L., Sberna, P. M., & Norte, R. A. (2026). High-Stress Si_3N_4 Reflective Membranes Monolithically Integrated With Cavity Bragg Mirrors. *Advanced Optical Materials*, *14*(39), Article e71871. https://doi.org/10.1002/adom.71871

Important note
To cite this publication, please use the final published version (if applicable).
Please check the document version above.

Copyright
In case the licence states “Dutch Copyright Act (Article 25fa)”, this publication was made available Green Open Access via the TU Delft Institutional Repository pursuant to Dutch Copyright Act (Article 25fa, the Taverne amendment). This provision does not affect copyright ownership.
Unless copyright is transferred by contract or statute, it remains with the copyright holder.

Sharing and reuse
Other than for strictly personal use, it is not permitted to download, forward or distribute the text or part of it, without the consent of the author(s) and/or copyright holder(s), unless the work is under an open content license such as Creative Commons.

Takedown policy
Please contact us and provide details if you believe this document breaches copyrights.
We will remove access to the work immediately and investigate your claim.

This work is downloaded from Delft University of Technology.

Check for updates

Advanced Optical Materials

ADVANCED OPTICAL MATERIALS
www.advopticalmat.de

RESEARCH ARTICLE OPEN ACCESS

High-Stress Si_3N_4 Reflective Membranes Monolithically Integrated With Cavity Bragg Mirrors

Megha Khokhar[1] | Lucas Norder[1] | Paolo M. Sberna[2] | Richard A. Norte[1]

[1]Department of Precision and Microsystems Engineering, Delft University of Technology, Delft, the Netherlands | [2]Else Kooi Laboratory, Faculty of Electrical Engineering, Mathematics and Computer Science, Delft University of Technology, Delft, the Netherlands

Correspondence: Paolo M. Sberna (p.m.sberna@tudelft.nl) | Richard A. Norte (r.a.Norte@tudelft.nl)

Received: 18 May 2026 | **Revised:** 14 September 2026 | **Accepted:** 19 September 2026

Keywords: acoustics | distributed Bragg reflector | fabrication | materials science | optical cavity | optoelectronics | optomechanics | photonics | resonator | silicon nitride

ABSTRACT

High-stress silicon nitride (Si_3N_4) membranes represent the state-of-the-art for cavity optomechanics, combining ultralow dissipation, optical transparency, and full compatibility with wafer-scale nanofabrication. Yet their integration into high-finesse optical cavities has remained difficult, typically requiring bonding or alignment-sensitive assembly that limits scalability and long-term stability. Here, we introduce a monolithic, wafer-level integration strategy that directly suspends high-stress Si_3N_4 photonic-crystal membranes above thermally compatible SiN/SiO_2 distributed Bragg reflectors (DBRs) capable of withstanding the high temperatures required for stoichiometric Si_3N_4 growth. An amorphous-silicon sacrificial layer and stiction-free plasma undercut yield vertically coupled cavities with sub-micron spacing—forming self-aligned resonators within seconds of release. Owing to the intrinsic tensile stress, the suspended membranes exhibit atomic-scale sagging, ensuring near-ideal cavity parallelism and long-term stability. Optical reflectivity measurements reveal cavity finesse above 4×10^2 with wavelength-scale gaps between mirrors. Mechanical ringdown measurements show $Q_{\mathrm{mech}} > 10^5$, indicating that DBR integration preserves the low-dissipation character of high-stress Si_3N_4. This supports straightforward extension to many high-Q nanomechanical architectures. The resulting Si_3N_4–DBR platform unites optical and mechanical coherence with high fabrication yield and design flexibility, enabling scalable optomechanical devices for precision sensing and quantum photonics.

1 | Introduction

Cavity optomechanics, which leverages the interaction between light and mechanical motion in resonant systems, has emerged as a pivotal platform for both fundamental studies and precision sensing technologies [1, 2]. At its simplest, it consists of an optical cavity with one of its mirrors being movable. The mirror's motion modulates the cavity field, enabling exquisite readout of displacement and forces. Confining light within small volumes with high-finesse cavities further amplifies these effects, enabling ground-state cooling [3], quantum squeezing [4], and ultra-sensitive force [5] and some of the most sensitive displacement detection achieved in science [6]. Achieving such performance requires extreme optical and mechanical coherence: the cavity must maintain high finesse, and the mechanical element must exhibit ultralow mechanical dissipation and strong optomechanical coupling. To approach these limits, the movable mirror should combine high optical quality (high reflectivity and low curvature) with low mechanical loss, which in practice favors lightweight, high-stress membranes that can be engineered for minimal coupling to their supports.

Among available materials for such reflectors, high-stress silicon nitride (Si_3N_4) membranes have emerged as a state of the art

This is an open access article under the terms of the Creative Commons Attribution License, which permits use, distribution and reproduction in any medium, provided the original work is properly cited.
© 2026 The Author(s). *Advanced Optical Materials* published by Wiley-VCH GmbH

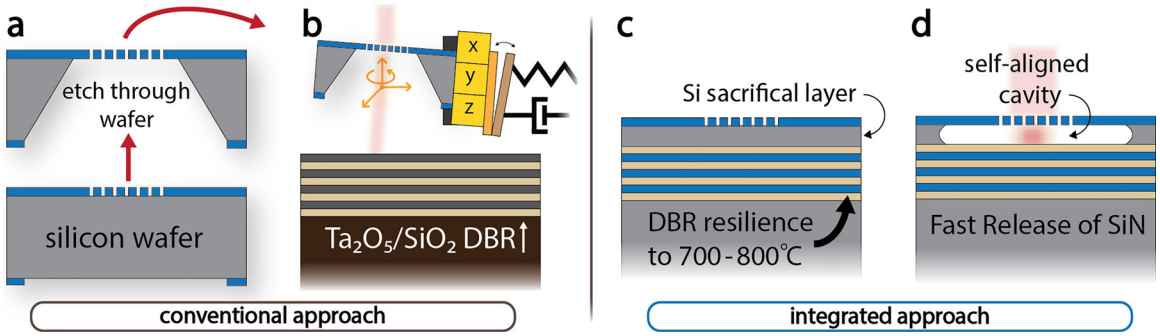


FIGURE 1 | Conventional fabrication of Si_3N_4 membranes versus integrated approach. (a) conventional fabrication of Si_3N_4 membranes for optical access requires deep etches through the chip, which are complex, delicate, and leave residues that must be subsequently cleaned off. (b) Complex alignment infrastructure to align with conventional DBR to form cavity. (c) Integrated approach deposits high-stress Si_3N_4 at high temperatures over Si sacrificial layer and DBR made from SiO_2 and Si_3N_4. A few second undercut of Si layer suspended high-stress Si_3N_4 photonic crystal membranes above DBR to form self-aligned, monolithic optomechanical cavity with a high Q_{mech}.

for room-temperature optomechanics [7]. Their combination of large built-in tensile stress [8], ultralow optical absorption at telecom wavelengths (parts per billion) [9], and wafer-scale CMOS manufacturing has enabled exceptional optomechanical performance (Q_{mech}) [10–15]. As a result, Si_3N_4 membranes enable attonewton-level force sensing, chip-scale inertial navigation [16], mechanical frequency combs [17], and quantum state preparation at room temperature [18]. Their versatility has enabled a wide range of nanomechanical geometries, including: strings [14, 19–24], drumheads [10, 25–28], phononic-crystal resonators [11, 13, 15, 29, 30], and trampoline membranes [5, 12, 31, 32]. All examples exhibit record-low damping and strong isolation from room temperature thermomechanical noise.

A key ingredient behind this performance is the high-temperature Low Pressure Chemical Vapor Deposition (LPCVD) required to form stoichiometric Si_3N_4 with gigapascal (GPa) tensile stress and parts-per-billion optical absorption [9]. These elevated temperatures achieve stoichiometry that suppresses absorption and yields a mechanical loss tangent among the lowest of any nanomechanical material in the kHz–MHz bending regime. While Si_3N_4 resonators already exhibit the highest Q_{mech} at room temperature, their quality factor increases even further at cryogenic temperatures [33–37], reinforcing their role as a uniquely powerful platform for both quantum and precision sensing at all temperatures.

Such extreme mechanical sensitivity, however, demands an equally stable optical interface for readout. Achieving sub-nanometer alignment between reflective Si_3N_4 membranes and conventional mirrors requires exceptional mechanical precision and thermal stability, typically enforced by extensive alignment infrastructure [38–46]. As shown in Figure 1a,b, existing implementations often rely on fabrication schemes that etch completely through the Si_3N_4 chip to open an optical access window [47], followed by manual alignment of the membrane with an external cavity structure. These conventional approaches are delicate, time-consuming, and difficult to scale or package.

Recent efforts to integrate high-performance nanomechanical mirrors above distributed Bragg reflectors (DBRs) have explored sacrificial-layer deposition strategies, as demonstrated in III–V systems [48]. However, III–V platforms remain limited by small wafer formats, CMOS incompatibility, and mechanical properties that degrade over time. Extending similar integration schemes to Si_3N_4 has been fundamentally constrained by material incompatibility: the high temperatures (≈700°C–800°C) required for stoichiometric, high-stress Si_3N_4 growth exceed the thermal budget of conventional Ta_2O_5/SiO_2 DBRs, leading to film degradation and delamination. Attempts to directly bond Si_3N_4 membranes on mirrors have not maintained a high Q_{mech} [43, 49] and still required tedious alignment. These limitations have prevented the realization of a scalable, monolithic optomechanical cavity platform that maintains the exceptional optical and mechanical performance of Si_3N_4 membranes. Ultra-short cavity lengths have been long-sought for their ability to enhance optomechanical coupling in ways that depart from longer free-space cavities [45, 48]

In this work, we overcome these long-standing challenges by introducing a monolithic cavity platform that directly integrates a suspended high-stress Si_3N_4 membrane above a thermally robust, low-loss LPCVD SiO_2/Si_3N_4 DBR. Using a thermally stable amorphous-silicon sacrificial layer and a stiction-free dry plasma undercut, we achieve sub-micron cavity gaps between membrane reflector and DBR. These are self-aligned with nanoscale precision and are among the shortest free-space optomechanical cavities to date utilizing reflective Si_3N_4 membranes [45, 48, 49]. The suspended membranes with about 1 GPa of tensile stress exhibit picometer-scale sag on the order of an atomic radius, naturally producing parallel optical interfaces and high fabrication yield. This establishes a scalable route to compact, high-coherence Si_3N_4 cavity optomechanics without the alignment and assembly bottlenecks of conventional membrane-in-the-middle systems.

2 | Design and Optical Optimization of an Integrated Optomechanical Cavity

Optical cavity readout is achieved by vertically coupling a mechanically compliant Si_3N_4 photonic crystal (PtC) membrane to a high-reflectivity DBR, forming a compact Fabry–Pérot cavity (Figure 2a). In this geometry, the suspended PtC serves as the partially transmitting top mirror and the DBR as the highly

21951071, 0, Downloaded from https://advanced.onlinelibrary.wiley.com/doi/10.1002/adom.71871, Wiley Online Library on [22/10/2026]. See the Terms and Conditions (https://onlinelibrary.wiley.com/terms-and-conditions) on Wiley Online Library for rules of use; OA articles are governed by the applicable Creative Commons License

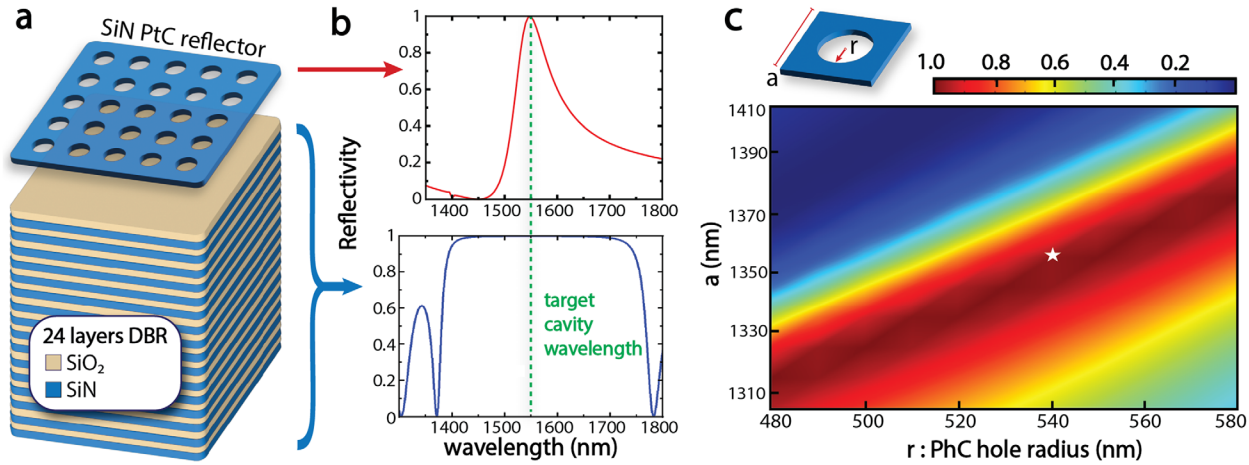


FIGURE 2 | Design and optical optimization of the integrated Si_3N_4–DBR cavity. (a) Schematic of the cavity structure showing a high-stress Si_3N_4 PtC membrane suspended above a 24-layer Si_3N_4/SiO_2 distributed Bragg reflector (DBR). (b) Simulated reflectivity spectra of the PtC membrane (red) and the DBR (blue), showing their overlap at the target cavity wavelength of 1550 nm (green dashed line). (c) Simulated reflectivity contour map of the PtC as a function of lattice constant a and hole radius r, indicating the design point (white star) used for fabrication. The zig-zag features along the high-reflectivity band arise from finite sampling of the parameter sweep and do not reflect any physical discontinuity in the PtC response.

reflective bottom mirror, while the sub-micron air gap between them defines the optical cavity. Small membrane displacements modulate the cavity resonance frequency, enabling sensitive interferometric readout. The corresponding optomechanical coupling strength, $G = \partial\omega_c/\partial x$, increases as the optical mode volume is reduced, so tighter vertical confinement and smaller cavity gaps enhance displacement-to-frequency transduction.

First, the DBR is designed. We use alternating SiO_2 ($n_1 = 1.44$) and Si_3N_4 ($n_2 = 2.0$) quarter-wave layers centered at 1550 nm. Thicknesses of 269 nm (SiO_2) and 194 nm (Si_3N_4) yield constructive optical interference and a simulated peak reflectivity of $\approx 99.91\%$ for a 24-layer stack with total thickness ≈ 5.8 μm. The topmost layer is SiO_2, which improves selectivity during the SF_6 release step, minimizes surface roughness, and ensures that the DBR remains optically pristine throughout processing. A representative DBR spectrum is shown in Figure 2b.

The suspended membrane acts as a lithographically tunable photonic mirror: adjusting its PtC geometry allows fine control over its reflectivity and over the wavelength at which it overlaps the DBR stopband. We use a 200-nm-thick high-stress Si_3N_4 film, which balances reflectivity with mechanical dissipation (thinner membranes improve Q_{mech} but reduce achievable optical reflectivity).

Finite-element simulations (COMSOL) were used to obtain the reflectivity of the PtC by sweeping hole radius r and lattice constant a near the 1550 nm design point. The resulting reflectivity map (Figure 2c) displays a narrow diagonal band of high reflectance in the hole-radius–lattice-constant plane, corresponding to constructive out-of-plane interference. The geometry marked by the white star maximizes reflectivity while remaining robust against lithographic tolerances.

Because the photonic crystal mirror relies on in-plane periodicity, it is naturally polarization dependent and its reflectivity varies with the incident beam's divergence. Larger, less focused beams sample more periods with a narrower in-plane k-distribution, improving effective reflectance. In contrast, the DBR has only vertical periodicity and is polarization insensitive, providing uniform broadband reflectivity.

To model the combined cavity, rigorous coupled-wave analysis (RCWA) is used. In this simulation, realistic fabrication deviations from nominal values are included. Simulations reproduce the measured response using the following representative parameters $a = 1.36$ μm, $r = 0.557$ μm, $t_{SiN} = 193$ nm, $t_{SiO} = 271$ nm, $n_{SiN} = 2.09$, $n_{SiO} = 1.42$, cavity spacing $t_{cav} \approx 0.95$ μm, and final Si_3N_4 membrane thickness $t_{PtC} = 191$ nm. Thickness variations in the LPCVD films (typically within ~ 5 nm for our calibrated process) shift the PtC resonance in wavelength rather than reducing its reflectivity, and the broad DBR stopband maintains overlap, so cavity finesse is not significantly affected.

Overall, the DBR provides a thermally robust, broadband mirror whose broad stopband does not constrain the resonance wavelength; the cavity resonance is instead set jointly by the fixed air-gap length and the reflection phase of the lithographically defined PtC. Because the membranes are patterned lithographically, an array of devices with varying hole radius can be written on a single chip, all sharing the same gap, so that sweeping the radius across the array matches the resonance to the target wavelength without altering the fixed cavity length. Together they form a monolithic, self-aligned cavity with strong vertical confinement suitable for high-sensitivity optomechanical readout.

3 | Scalable Nanofabrication Using Dry Processing Techniques

To realize a robust, wafer-scale platform for monolithic optomechanical cavities, we developed a fabrication flow composed entirely of dry-processing steps (Figure 3a), with both top- and cross-sectional views shown for each stage. Eliminating liquids

21951071, 0, Downloaded from https://advanced.onlinelibrary.wiley.com/doi/10.1002/adom.71871, Wiley Online Library on [22/10/2026]. See the Terms and Conditions (https://onlinelibrary.wiley.com/terms-and-conditions) on Wiley Online Library for rules of use; OA articles are governed by the applicable Creative Commons License

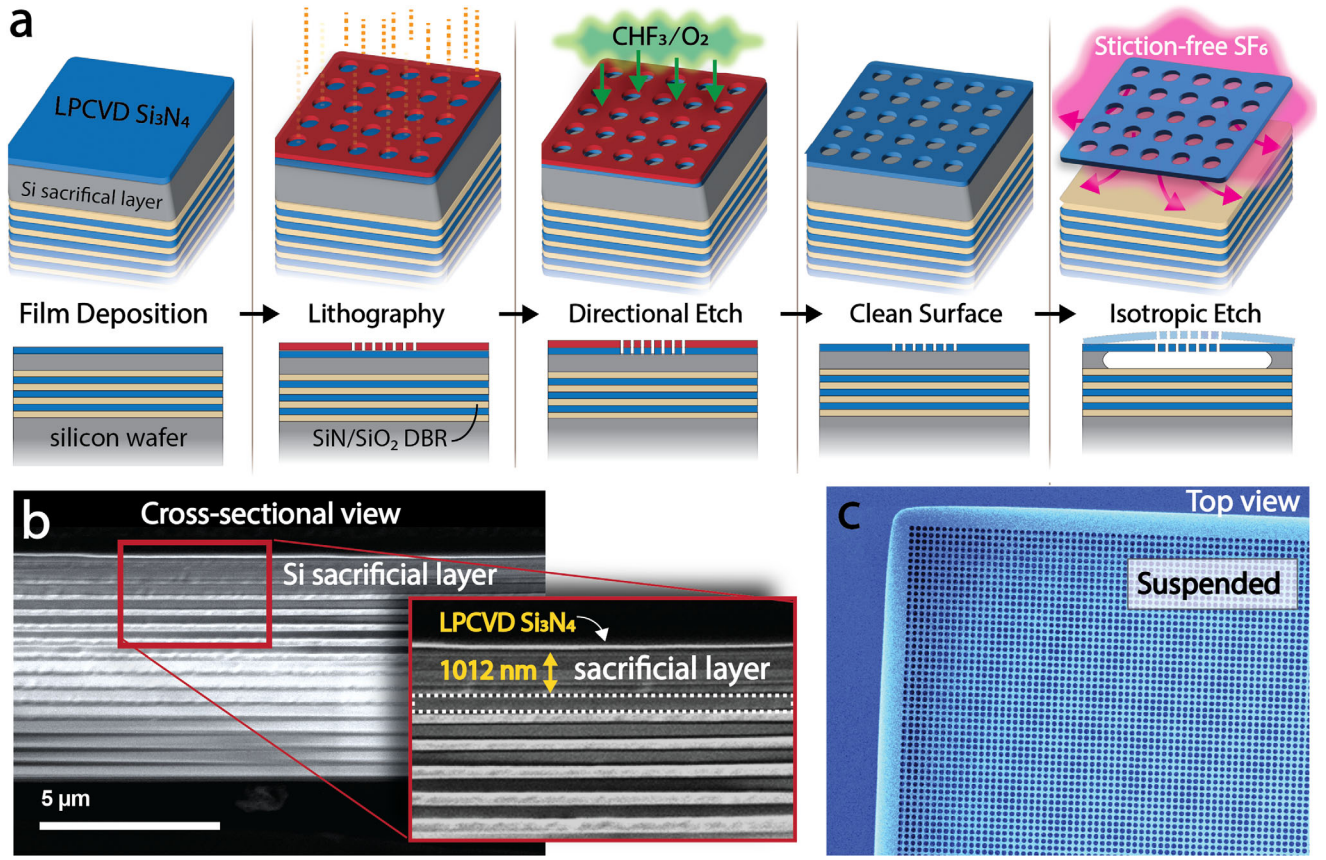


FIGURE 3 | High-yield fabrication of monolithic Si_3N_4–DBR optomechanical cavities. (a) Schematic fabrication flow with top and side views for each step: LPCVD growth of the Si_3N_4/SiO_2 DBR and amorphous-Si sacrificial layer; lithographic patterning of the Si_3N_4 membrane; directional CHF_3/O_2 etching; surface cleaning; and stiction-free isotropic SF_6 undercut to suspend the membrane. (b) Cross-sectional SEM showing the DBR stack, amorphous-Si sacrificial layer, and top Si_3N_4 membrane prior to release (inset: measured sacrificial-layer thickness ~1012 nm). The white dashed lines highlight the top SiO_2 layer of the DBR. (c) Top-view optical micrograph of the fully suspended membrane, demonstrating wafer-scale uniformity and clean release.

in the fabrication process avoids stiction and capillary forces, ensuring that the pristine optical and mechanical properties of high-stress Si_3N_4 are fully preserved.

The process begins with LPCVD deposition of the multilayer Si_3N_4/SiO_2 DBR on a silicon wafer. Because every layer is deposited at high temperature, the DBR maintains its structural stability and sharp interfaces throughout subsequent processing. A 1012 nm amorphous-Si sacrificial layer is then deposited by LPCVD. Because hydrogen desorbs above approximately 400°C, deposition at these temperatures results in negligible hydrogen incorporation, preventing blistering or bubble formation during the later high-temperature LPCVD Si_3N_4 step. Finally, a 200 nm stoichiometric Si_3N_4 layer is deposited to form the high-stress membrane and later patterned with holes to increase its reflectivity. The full deposition recipes are detailed in Methods.

The membrane pattern is defined using high-resolution electron-beam lithography. After exposure and development, the square-lattice PtC holes are transferred into the Si_3N_4 layer using a CHF_3/O_2 Inductively Coupled Plasma Reactive Ion Etching (ICP-RIE) that provides anisotropic profiles and smooth sidewalls. Residual resist is removed with N,N-dimethylformamide, followed by a piranha clean to eliminate organics and leave a chemically pristine membrane surface prior to suspension.

Suspension is achieved through a short isotropic SF_6 plasma undercut, which selectively removes the amorphous-Si layer while leaving both the membrane and DBR relatively unetched (Figure 3a). Because the release is fully dry, the process is inherently stiction-free, enabling the fabrication of high-aspect-ratio suspended nanostructures with minimal collapse or fracturing [14, 15, 50]. The SF_6 undercut produces exceptionally clean cavity interfaces, uniform air gaps, and high repeatability across full wafers [51]. The suspended membrane is thinned slightly from its 200 nm deposition target during the SF_6 undercut, which etches a few nanometers from each face of the high-aspect-ratio membrane, giving a final thickness of ~191 nm; the unsuspended DBR layers are unaffected. Importantly, this dry-release method has repeatedly been shown to produce nanomechanical devices with some of the lowest mechanical and optical losses to date, and with high-fidelity agreement between simulated and measured dissipation—performance that is difficult to achieve with liquid-based etches such as KOH, which can require hours of through-wafer etching to obtain optical access. In contrast, our cavities are formed in tens of seconds, immediately yielding a fully aligned Si_3N_4 membrane–DBR cavity; this represents a fundamental shift

21951071, 0, Downloaded from https://advanced.onlinelibrary.wiley.com/doi/10.1002/adom.71871, Wiley Online Library on [22/10/2026]. See the Terms and Conditions (https://onlinelibrary.wiley.com/terms-and-conditions) on Wiley Online Library for rules of use; OA articles are governed by the applicable Creative Commons License

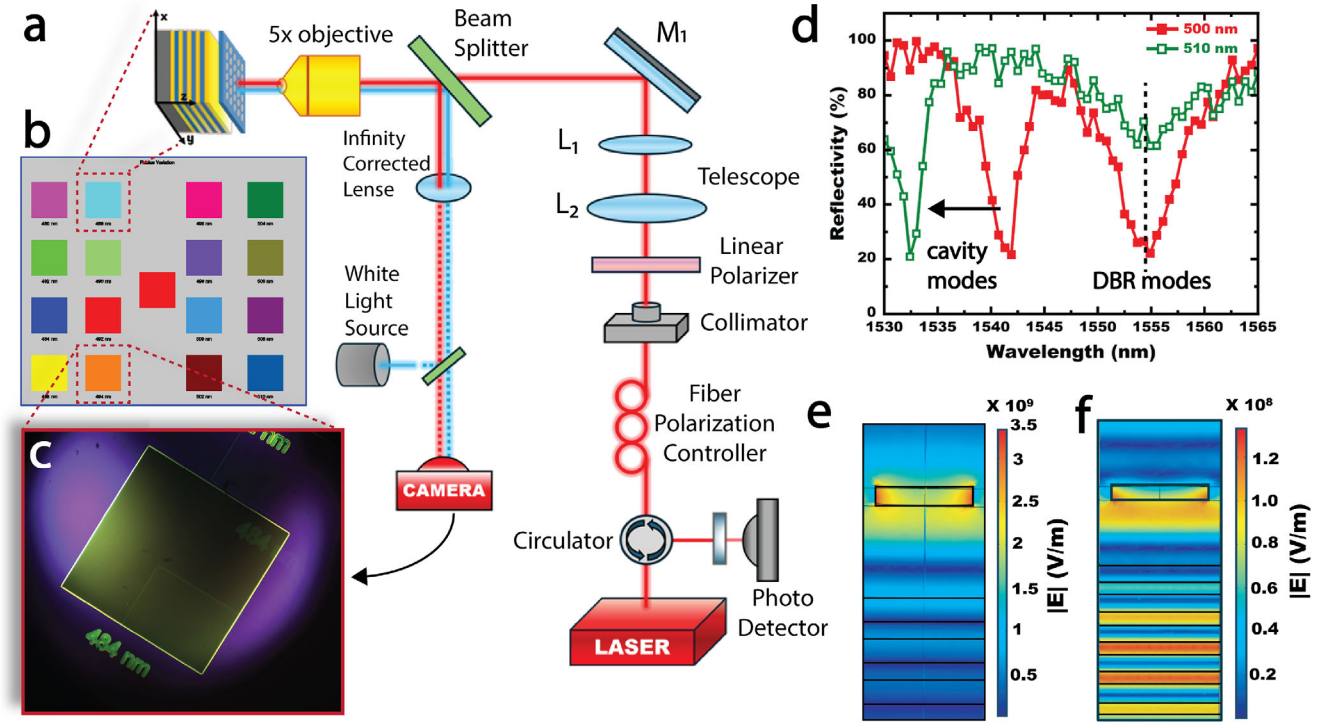


FIGURE 4 | Optical characterization of the integrated Si_3N_4–DBR cavity using broadband reflectivity measurements. (a) Schematic of the micro-reflectivity setup used for cavity measurements, combining a tunable IR laser for reflectivity spectroscopy with a white-light camera path for alignment. (b) Layout of the fabricated chip showing an array of sixteen $1 \times 1\,mm^2$ suspended PtC membranes with lithographically varied hole radii, plus a central DBR-only reference region. (c) Camera image used during alignment, showing a suspended Si_3N_4 membrane under white-light illumination. The IR probe beam is aligned to the membrane center via the optical path and is not directly visible in the white-light image. (d) Measured reflectivity spectra for two membrane designs (500 and 510 nm hole radii). The cavity mode shifts with radius, while the DBR-associated mode remains fixed. (e) Simulated electric-field distribution of the vertically confined cavity mode formed in the air gap. (f) Simulated electric-field distribution of the DBR-associated photonic band-edge mode, confined mainly within the DBR stack. The black box in (e,f) outlines an air hole in the patterned membrane.

in how state-of-the-art membrane materials are integrated with readily available optical readout systems.

Cross-sectional SEM images (Figure 3b) show the multilayer DBR, the sacrificial layer, and the sharpness of the interfaces produced by the LPCVD stack. Top-view images (Figure 3c) show fully suspended membranes with uniform PtC patterns. The residual tensile stress of ≈1 GPa keeps the films taut, flat, and robust during handling and optical probing, with nanoscale sag across millimeter-scale spans [52], producing cavity parallelism between the membrane and DBR that would be infeasible to recreate with conventional alignment schemes as shown in Figure 1b.

Together, these dry-processing steps provide a high-yield, wafer-scale route to monolithic membrane–DBR cavities with robust structural integrity. We now show that the platform delivers more than mechanically surviving membranes: it also preserves strong optical cavity performance and low mechanical dissipation.

4 | Optical Cavity Characterization

To evaluate the optical performance of the integrated Si_3N_4 membrane–DBR cavity, we performed micro-reflectivity measurements using the setup shown in Figure 4a. A tunable diode laser (1530–1620 nm) is routed through a fiber polarization controller, a collimator, a linear polarizer, and a telescope (L_1, L_2) that sets the beam size, then focused onto the membrane using a nominal 5× objective whose aperture is strongly underfilled, giving an effective illumination numerical aperture $NA_{eff} \simeq 0.003$ (beam waist $\simeq 162\ \mu m$) so that the membrane is probed at near-normal incidence. Reflected light returns through the same optical path and is routed to a photodiode via a circulator. Transmission measurements are not accessible in this geometry, as the DBR is designed for near-unity reflectivity and the substrate is single-side-polished. Reflection spectroscopy is therefore the natural characterization method and has the added benefit of being compatible with arbitrarily thick substrates, which are known to improve mechanical quality factors [12]. A white-light illumination path and camera are integrated into the beam path, enabling real-time imaging and precise alignment of the membrane under test.

To allow systematic optical characterization, the chip contains an array of sixteen 1×1 mm^2 suspended membranes with lithographically varied PtC radii, as illustrated in Figure 4b. A reference region without a membrane (center tile) provides direct measurement of the bare DBR reflectivity. During measurement, the camera image (Figure 4c) is used to position the IR probe spot on the suspended membrane while visually confirming membrane integrity and avoiding edges or defects.

21951071, 0, Downloaded from https://advanced.onlinelibrary.wiley.com/doi/10.1002/adom.71871, Wiley Online Library on [22/10/2026]. See the Terms and Conditions (https://onlinelibrary.wiley.com/terms-and-conditions) on Wiley Online Library for rules of use; OA articles are governed by the applicable Creative Commons License

Representative reflectivity spectra for two PtC radii are shown in Figure 4d, each exhibiting two prominent dips. The short-wavelength feature (1535–1545 nm) is the vertically confined cavity mode: it blue-shifts as the hole radius increases (500 nm vs. 510 nm), reflecting the change in the membrane's effective refractive index as the air fill fraction increases. The longer-wavelength dip near 1555 nm originates from the DBR stack and remains spectrally fixed across all membrane designs, confirming that it is governed by the multilayer mirror rather than the patterned membrane. This demonstrates spectral tunability across devices on a single chip: the membrane governs the cavity-mode position while the DBR provides a stable, broadband bottom mirror unaffected by lithographic variation.

To identify the physical origin of these resonances, we performed finite-element simulations of the electric-field distribution (Figure 4e,f). At the cavity resonance wavelength, the field is strongly localized within the air gap, forming a vertically confined Fabry–Pérot mode with a standing-wave pattern between the high-reflectivity DBR and the PtC membrane (Figure 4e). This mode exhibits a narrow linewidth with measured FWHM of 2.5 nm, corresponding to an optical quality factor $Q_{opt} \approx 600$ and a finesse of ≈ 470. The field is not a laterally uniform planar mode but is modulated in-plane and enhanced near the boundaries of the patterned membrane, reflecting the hybrid character of the cavity mode and the in-plane response of the photonic crystal; similar field distributions have been reported for comparable suspended-PtC/DBR microcavities [48].

The longer-wavelength feature corresponds to a DBR mode that arises when light scattered by the patterned membrane acquires non-planar wavevectors. Although a bare DBR strongly reflects normally incident plane waves, the proximity of the PtC membrane introduces lateral scattering that generates off-axis and higher-order k-components. These components can penetrate the multilayer stack and form a band-edge–like optical mode primarily confined within the DBR, with only weak, evanescent coupling back into the membrane (Figure 4f). Because this resonance is governed by in-plane scattering dynamics rather than the vertical cavity spacing, its spectral response remains fixed as the hole radius is varied. As a result, it appears as a broader, geometry-insensitive feature (FWHM 6.1 nm, $Q_{opt} \approx 250$) in the reflectivity spectrum. Simulated sweeps of hole diameter and cavity length (Figure S1) confirm this assignment: the short-wavelength mode shifts with cavity length, as expected for a vertically confined mode and not for an in-plane slab resonance, while the DBR feature remains fixed in both sweeps.

Overall, the combined experimental and simulated results confirm that the integrated platform functions as a stable, tunable, high-finesse cavity. The cavity mode's confinement in the air gap between the membrane and DBR makes it ideal for interferometric displacement sensing, while the coexistence of membrane and DBR modes offers opportunities for hybrid photonic–optomechanical architectures.

5 | Mechanical Characterization

In the past several years, the isotropic SF_6 plasma undercut used here has emerged as one of the most powerful release techniques for Si_3N_4, enabling devices with Q_{mech} approaching 10^9–10^{10} on standard silicon substrates. However, it has never been established whether integrating Si_3N_4 with a multilayer DBR—containing dozens of interfaces, different acoustic impedances, and altered boundary conditions—introduces mechanical loss or degrades dissipation dilution. Demonstrating Q preservation is therefore essential before this integration platform can be used for state-of-the-art optomechanically engineered geometries.

To evaluate this, we characterized the same suspended membrane–DBR cavities described above using laser Doppler vibrometry (LDV) under high vacuum ($\approx 10^{-6}$ mbar). The membrane was actuated by a piezoelectric shaker mounted to the sample holder, and the spatial velocity maps were obtained by raster-scanning the focused LDV spot across the membrane. Figure 5a shows the measured out-of-plane velocity field of the fundamental membrane mode, exhibiting the expected symmetric displacement profile. A broadband sweep (Figure 5b) identifies the fundamental mechanical resonance near 259 kHz and several higher-order modes extending to 1 MHz. To measure the ringdown, the drive was applied near the fundamental resonance and then abruptly switched off; the resulting decay (Figure 5c) yields a mechanical quality factor $Q_{mech} = 3.0 \times 10^5$, demonstrating low intrinsic damping and strong stress dilution.

Because the membranes used here are ~200 nm thick (i.e., chosen to ensure high optical reflectivity), these Q_{mech} values are naturally lower than those achievable with ultra-thin (20 nm) Si_3N_4 films used to maximize Q_{mech}, reflecting the trade-off between optical reflectivity, which favors thicker films, and mechanical dissipation, which favors thinner ones. Thicker mirrors are required for the PtC reflectivity, but multi-thickness designs can decouple these requirements (e.g., thick mirror region with thin, stress-diluted clamping) [4, 12]. Thus, it is important not only to measure the Q_{mech} of this simple square-lattice membrane, but to verify that DBR integration does not introduce additional loss. If Q_{mech} is preserved in this geometry, the platform can support the full family of high-Q_{mech}, phononic-engineered, soft-clamped, or tethered designs known to reach 10^8–10^{10}.

To assess the mechanical impact of DBR integration, we first identified the highest-Q_{mech} device on the DBR-integrated chip, corresponding to a hole radius of 484 nm. We then fabricated the nominally identical chip layout without DBR integration and directly compared the same membrane design (Figure 4b). The DBR-integrated membrane exhibited a fundamental frequency of 259 kHz and $Q_{mech} = 3.0 \times 10^5$, while the corresponding membrane on silicon without DBR showed a slightly higher frequency of 290 kHz and $Q_{mech} = 3.8 \times 10^5$. The frequency shift is consistent with small variations in film thickness and thermal-expansion stresses associated with the DBR structure. Across the measured device sets (three PtC+DBR and five PtC-only devices, fundamental mode only, excluding visibly defective ones), the average mechanical quality factors were $\langle Q_{mech} \rangle = 1.3 \times 10^5$ for the PtC+DBR devices and $\langle Q_{mech} \rangle = 4.6 \times 10^5$ for the PtC-only devices, indicating that the integrated structures remain within the same order of magnitude in mechanical coherence. The measured quality factors ranged from 3.5×10^4 to 3.0×10^5 and from 6.8×10^4 to 9.1×10^5, respectively; the comparable spread in both sets indicates that this scatter is intrinsic to high-Q_{mech} membrane measurements rather than introduced by DBR

21951071, 0, Downloaded from https://advanced.onlinelibrary.wiley.com/doi/10.1002/adom.71871, Wiley Online Library on [22/10/2026]. See the Terms and Conditions (https://onlinelibrary.wiley.com/terms-and-conditions) on Wiley Online Library for rules of use; OA articles are governed by the applicable Creative Commons License

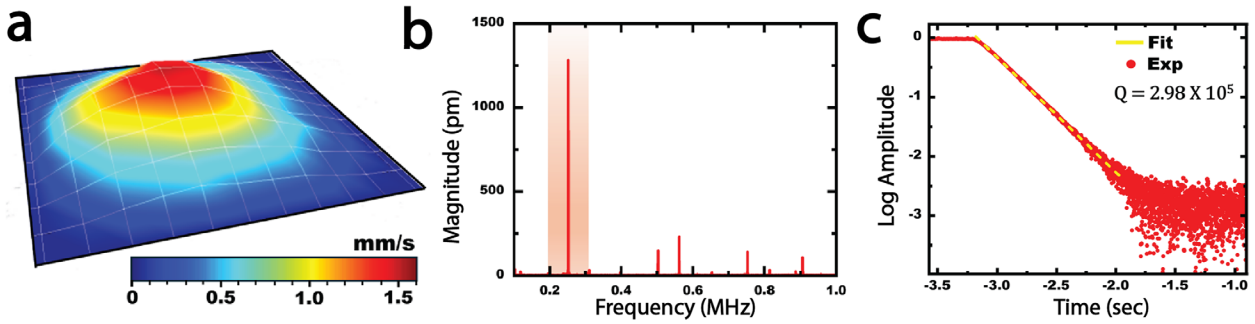


FIGURE 5 | Mechanical characterization of the suspended Si_3N_4 membrane integrated with a DBR platform. (a) Out-of-plane velocity map of the fundamental membrane mode measured by laser Doppler vibrometer. (b) Frequency-domain spectrum showing the fundamental resonance and higher-order modes. (c) Mechanical ringdown measurement of the fundamental mode, with an exponential fit (yellow) used to extract Q_{mech}.

integration. Crucially, no catastrophic degradation in Q_{mech} was observed upon DBR integration. Unlike soft-clamped modes, the fundamental modes of square-lattice membranes are strongly coupled to the substrate and therefore maximize chip-based loss channels, making them a stringent reference for assessing additional dissipation introduced by the DBR stack [53].

These measurements demonstrate that the Si_3N_4/SiO_2 DBR introduces little additional mechanical loss. The SF_6 release process preserves the dissipation characteristics of the membrane even on a multilayer mirror substrate, confirming full compatibility with high-stress Si_3N_4. This establishes the platform as a mechanically benign integration scheme capable of supporting the highest-Q geometries developed in the community while simultaneously enabling a compact, high-finesse optical cavity.

6 | Discussion

We have presented a scalable, CMOS-compatible fabrication strategy that monolithically integrates high-stress Si_3N_4 membranes with broadband distributed Bragg reflectors (DBRs) using a wafer-level, lithography-defined process. This platform removes a longstanding bottleneck in cavity optomechanics by eliminating bonding, through-wafer etching, and precision alignment. Instead, a stiction-free gas-phase undercut defines a vertically self-aligned cavity with uniform sub-micron membrane–DBR spacing. With a cavity length of ~950 nm, close to half the operating wavelength, this forms a single-longitudinal-mode cavity whose free spectral range is comparable to the optical frequency itself. Vertical optomechanical coupling is especially well suited to Si_3N_4, as its highest-Q_{mech} resonators exploit out-of-plane flexural modes defined by ultrathin film thicknesses (≈20 nm), which are straightforward to realize by deposition but extremely challenging to achieve through lateral nanolithography [51].

A central materials advance is the use of alternating LPCVD Si_3N_4 and SiO_2 layers to form a thermally robust DBR. Although the refractive-index contrast is lower than in Ta_2O_5/SiO_2 stacks, the LPCVD process yields low optical absorption and remains stable through the 700°C–800°C required for stoichiometric high-stress Si_3N_4 deposition.

Optical and mechanical characterization confirms that integration preserves the essential performance of the Si_3N_4 platform. Mechanical ringdown measurements show $Q_{mech} > 10^5$, comparable to non-integrated membranes, while reflectivity spectra show cavity finesses above 400, demonstrating integrated optical functionality suitable for interferometric readout. Although our demonstration uses relatively thick (~200 nm) square-lattice membranes rather than geometries optimized for record Q_{mech}, the DBR process adds little mechanical loss compared to identical devices without DBR. The flat–flat cavity geometry does not limit the finesse under our illumination conditions, as the effective beam waist of ~162 μm gives a Rayleigh range far exceeding the cavity length, making diffraction and walk-off losses negligible. The finesse is therefore set by optical loss within the cavity, and our measurements reflect the losses of the integrated system as a whole rather than isolating either mirror. The most likely contributions are perhaps non-ideal PtC reflectivity at the realized cavity wavelength, together with scattering from interface roughness, which accumulates over the many DBR layers such that the uppermost layers nearest the cavity are the roughest and contribute most to scattering loss. Reducing interfacial roughness and improving membrane reflectivity together represent a clear path to higher finesse; introducing intermediate polishing steps between depositions is one route to reducing roughness, at increased process cost. Separating these contributions and characterizing the optomechanical coupling and cooperativity are natural next steps toward quantum-regime operation.

The fabrication route is broadly compatible with the wider ecosystem of Si_3N_4 resonators used in cavity optomechanics, including reflective phononic membranes [41], trampolines [12], hierarchical metamaterials, and high-aspect-ratio resonators [50]. It is also well suited to thick-substrate implementations, which are known to improve Q_{mech} for modes without soft clamping [12, 53, 54], since the SF_6 gas-phase release suspends membranes on millimeter-scale substrates in seconds while avoiding the stiction, bowing, and poor yield associated with wet-etch access through thick chips [31]. Previous strategies based on locally thickening the mirror region while thinning the clamping region to tens of nanometers [4, 12] should therefore be naturally extendable to this platform.

More broadly, the platform is compatible with the ultra-high-aspect-ratio geometries enabled by high-stress Si_3N_4. Recent work has shown that centimeter-scale PtC reflectors with nanometer thickness and billions of holes can be fabricated with exceptional flatness [50]; at these scales, larger beam diameters can sustain

21951071, 0, Downloaded from https://advanced.onlinelibrary.wiley.com/doi/10.1002/adom.71871, Wiley Online Library on [22/10/2026]. See the Terms and Conditions (https://onlinelibrary.wiley.com/terms-and-conditions) on Wiley Online Library for rules of use; OA articles are governed by the applicable Creative Commons License

high reflectivity even for thinner membranes [55]. Although we demonstrate a flat–flat cavity here, PtC structures with radially varying hole geometries can also impart effective curvature [56, 57], offering future opportunities for transverse-mode engineering, reduced sensitivity to lateral misalignment, and lower clipping loss. Such radially varying designs generally involve a trade-off, however, since maintaining the ultra-high reflectivity of uniform photonic crystals while imparting curvature is challenging and typically increases membrane transmission, which would reduce cavity finesse and cooperativity.

Taken together, this monolithic platform transforms a delicate, alignment-limited cavity optomechanical architecture into a robust and manufacturable one. By preserving the strong optical and mechanical performance of high-stress Si_3N_4 while replacing complex assembly with a simple self-aligned process, it provides a practical route toward scalable precision sensing, integrated photonics, and next-generation quantum technologies.

7 | Methods

The DBR multilayer was fabricated by alternating low-pressure chemical vapor deposition (LPCVD) of SiO_2 and low-stress silicon nitride layers. The oxide films were deposited in a horizontal hot-wall LPCVD furnace at 700°C and a pressure of 150 mTorr, using vaporized tetraethyl orthosilicate (TEOS) as the precursor. Low-stress silicon nitride layers were deposited in a similar furnace by introducing a mixture of NH_3 and dichlorosilane (DCS), with a fixed NH_3/DCS flow ratio of 0.19, corresponding to a Si-rich regime. The nitride deposition was carried out at 860°C and 150 mTorr.

LPCVD was preferred over plasma-enhanced CVD (PECVD) for nitride deposition due to the negligible hydrogen incorporation associated with the former technique. The resulting low hydrogen content confers excellent thermal stability to the films, preventing significant stress variations as well as cracking or delamination during subsequent deposition steps.

After completion of the DBR stack, a 1-μm-thick amorphous silicon layer was deposited by LPCVD, flowing SiH_4 at 560°C. Owing to the ultra-clean furnace and the deposition temperature, at which hydrogen desorbs, the resulting film has negligible hydrogen content, preventing blistering or delamination during the subsequent high-temperature nitride growth.

The topmost high-stress silicon nitride layer was subsequently deposited in the same furnace used for the DBR nitride layers, but with a substantially higher NH_3/DCS flow ratio corresponding to stoichiometric conditions. In this case, the deposition temperature and pressure were set to 700°C and 150 mTorr, respectively.

Acknowledgments

We thank Mohammadjavad Ebrahimipour and Juan Lizarraga Lallana for experimental help and Gerard Verbiest, Peter Steeneken, Andrea Cupertino and Dalziel Wilson for thoughtful comments. This work has received funding from the EMPIR programme co-financed by the Participating States and from the European Union's Horizon 2020 research and innovation programme (No. 17FUN05 PhotoQuant). This publication is part of the project, Probing the physics of exotic superconductors with microchip Casimir experiments (740.018.020) of the research programme NWO Start-up which is partly financed by the Dutch Research Council (NWO). Funded/Co-funded by the European Union (ERC, EARS, 101042855). Views and opinions expressed are however those of the author(s) only and do not necessarily reflect those of the European Union or the European Research Council. Neither the European Union nor the granting authority can be held responsible for them.

Conflicts of Interest

The authors declare no conflicts of interest.

Data Availability Statement

The data that support the findings of this study are available from the corresponding author upon reasonable request.

References

1. M. Aspelmeyer, T. J. Kippenberg, and F. Marquardt, "Cavity Optomechanics," *Reviews of Modern Physics* 86 (2014): 1391–1452, https://doi.org/10.1103/RevModPhys.86.1391.

2. B.-B. Li, L. Ou, Y. Lei, and Y.-C. Liu, "Cavity Optomechanical Sensing," *Nanophotonics* 10, no. 11 (2021): 2799–2832, https://doi.org/10.1515/nanoph-2021-0256.

3. M. Rossi, D. Mason, J. Chen, Y. Tsaturyan, and A. Schliesser, "Measurement-Based Quantum Control of Mechanical Motion," *Nature* 563, no. 7729 (2018): 53–58.

4. G. Huang, A. Beccari, N. J. Engelsen, and T. J. Kippenberg, "Room-Temperature Quantum Optomechanics Using an Ultralow Noise Cavity," *Nature* 626, no. 7999 (2024): 512–516.

5. C. Reinhardt, T. Müller, A. Bourassa, and J. C. Sankey, "Ultralow-Noise SiN Trampoline Resonators for Sensing and Optomechanics," *Physical Review X* 6 (2016): 021001, https://doi.org/10.1103/PhysRevX.6.021001.

6. B. P. Abbott, R. Abbott, T. D. Abbott, et al., "Observation of Gravitational Waves From a Binary Black Hole Merger," *Physical Review Letters* 116, no. 6 (2016): 061102.

7. N. J. Engelsen, A. Beccari, and T. J. Kippenberg, "Ultrahigh-Quality-Factor Micro-and Nanomechanical Resonators Using Dissipation Dilution," *Nature Nanotechnology* 19, no. 6 (2024): 725–737.

8. M. Xu, D. Shin, P. M. Sberna, et al., "High-Strength Amorphous Silicon Carbide for Nanomechanics," *Advanced Materials* 36, no. 5 (2024): 2306513.

9. A. T. Land, M. Dey Chowdhury, A. R. Agrawal, and D. J. Wilson, "Sub-PPM Nanomechanical Absorption Spectroscopy of Silicon Nitride," *Nano Letters* 24, no. 25 (2024): 7578–7583.

10. J. Thompson, B. Zwickl, A. Jayich, F. Marquardt, S. Girvin, and J. Harris, "Strong Dispersive Coupling of a High-Finesse Cavity to a Micromechanical Membrane," *Nature* 452, no. 7183 (2008): 72–75.

11. Y. Tsaturyan, A. Barg, E. S. Polzik, and A. Schliesser, "Ultracoherent Nanomechanical Resonators via Soft Clamping and Dissipation Dilution," *Nature Nanotechnology* 12, no. 8 (2017): 776–783.

12. R. A. Norte, J. P. Moura, and S. Gröblacher, "Mechanical Resonators for Quantum Optomechanics Experiments at Room Temperature," *Physical Review Letters* 116 (2016): 147202, https://doi.org/10.1103/PhysRevLett.116.147202.

13. A. H. Ghadimi, S. A. Fedorov, N. J. Engelsen, et al., "Elastic Strain Engineering for Ultralow Mechanical Dissipation," *Science* 360, no. 6390 (2018): 764–768.

14. D. Shin, A. Cupertino, M. H. de Jong, P. G. Steeneken, M. A. Bessa, and R. A. Norte, "Spiderweb Nanomechanical Resonators via Bayesian Optimization: Inspired by Nature and Guided by Machine Learning," *Advanced Materials* 34, no. 3 (2022): 2106248.

21951071, 0, Downloaded from https://advanced.onlinelibrary.wiley.com/doi/10.1002/adom.71871, Wiley Online Library on [22/10/2026]. See the Terms and Conditions (https://onlinelibrary.wiley.com/terms-and-conditions) on Wiley Online Library for rules of use; OA articles are governed by the applicable Creative Commons License

15. A. Cupertino, D. Shin, L. Guo, P. G. Steeneken, M. A. Bessa, and R. A. Norte, "Centimeter-Scale Nanomechanical Resonators With Low Dissipation," *Nature Communications* 15, no. 1 (2024): 4255.

16. A. G. Krause, M. Winger, T. D. Blasius, Q. Lin, and O. Painter, "A High-Resolution Microchip Optomechanical Accelerometer," *Nature Photonics* 6, no. 11 (2012): 768–772.

17. M. H. De Jong, A. Ganesan, A. Cupertino, S. Gröblacher, and R. A. Norte, "Mechanical Overtone Frequency combs," *Nature Communications* 14, no. 1 (2023): 1458.

18. D. Mason, J. Chen, M. Rossi, Y. Tsaturyan, and A. Schliesser, "Continuous Force and Displacement Measurement Below the Standard Quantum Limit," *Nature Physics* 15, no. 8 (2019): 745–749.

19. S. S. Verbridge, J. M. Parpia, R. B. Reichenbach, L. M. Bellan, and H. G. Craighead, "High Quality Factor Resonance at Room Temperature With Nanostrings Under High Tensile Stress," *Journal of Applied Physics* 99, no. 12 (2006): 124304.

20. P. Sadeghi, M. Tanzer, S. L. Christensen, and S. Schmid, "Influence of Clamp-Widening on the Quality Factor of Nanomechanical Silicon Nitride Resonators," *Journal of Applied Physics* 126, no. 16 (2019): 165108.

21. S. Schmid, K. Jensen, K. Nielsen, and A. Boisen, "Damping Mechanisms in High-Q Micro and Nanomechanical String Resonators," *Physical Review B–Condensed Matter and Materials Physics* 84, no. 16 (2011): 165307.

22. D. Hoch, X. Yao, and M. Poot, "Geometric Tuning of Stress in Predisplaced Silicon Nitride Resonators," *Nano Letters* 22, no. 10 (2022): 4013–4019.

23. Z. Li, M. Xu, R. A. Norte, A. M. Aragón, P. G. Steeneken, and F. Alijani, "Strain Engineering of Nonlinear Nanoresonators From Hardening to Softening," *Communications Physics* 7, no. 1 (2024): 53.

24. M. J. Bereyhi, A. Beccari, R. Groth, et al., "Hierarchical Tensile Structures With Ultralow Mechanical Dissipation," *Nature Communications* 13, no. 1 (2022): 3097.

25. E. Serra, B. Morana, A. Borrielli, et al., "Silicon Nitride MOMS Oscillator for Room Temperature Quantum Optomechanics," *Journal of Microelectromechanical Systems* 27, no. 6 (2018): 1193–1203.

26. D. J. Wilson, C. A. Regal, S. B. Papp, and H. J. Kimble, "Cavity Optomechanics With Stoichiometric SiN Films," *Physical Review Letters* 103 (2009): 207204, https://doi.org/10.1103/PhysRevLett.103.207204.

27. L. G. Villanueva and S. Schmid, "Evidence of Surface Loss as Ubiquitous Limiting Damping Mechanism in SiN Micro- and Nanomechanical Resonators," *Physical Review Letters* 113 (2014): 227201, https://doi.org/10.1103/PhysRevLett.113.227201.

28. S. Chakram, Y. S. Patil, L. Chang, and M. Vengalattore, "Dissipation in Ultrahigh Quality Factor SiN Membrane Resonators," *Physical Review Letters* 112 (2014): 127201, https://doi.org/10.1103/PhysRevLett.112.127201.

29. P.-L. Yu, K. Cicak, N. Kampel, et al., "A Phononic Bandgap Shield for High-Q Membrane Microresonators," *Applied Physics Letters* 104, no. 2 (2014): 023510.

30. C. Reetz, R. Fischer, G. G. Assumpcao, et al., "Analysis of Membrane Phononic Crystals With Wide Band Gaps and Low-Mass Defects," *Physical Review Applied* 12, no. 4 (2019): 044027.

31. R. A. Norte, *Nanofabrication for On-Chip Optical Levitation, Atom-Trapping, and Superconducting Quantum Circuits* (California Institute of Technology, 2015).

32. D. Høj, F. Wang, W. Gao, U. B. Hoff, O. Sigmund, and U. L. Andersen, "Ultra-Coherent Nanomechanical Resonators Based on Inverse Design," *Nature communications* 12, no. 1 (2021): 5766.

33. M. Yuan, M. A. Cohen, and G. A. Steele, "Silicon Nitride Membrane Resonators at Millikelvin Temperatures With Quality Factors Exceeding 108," *Applied Physics Letters* 107, no. 26 (2015): 263501.

34. T. Purdy, R. Peterson, P. Yu, and C. Regal, "Cavity Optomechanics With Si_3N_4 Membranes at Cryogenic Temperatures," *New Journal of Physics* 14, no. 11 (2012): 115021.

35. W.-H. Chuang, T. Luger, R. K. Fettig, and R. Ghodssi, "Mechanical Property Characterization of LPCVD Silicon Nitride Thin Films at Cryogenic Temperatures," *Journal of Microelectromechanical Systems* 13, no. 5 (2004): 870–879.

36. Y. Seis, T. Capelle, E. Langman, S. Saarinen, E. Planz, and A. Schliesser, "Ground State Cooling of an Ultracoherent Electromechanical System," *Nature Communications* 13, no. 1 (2022): 1507.

37. R. Fischer, N. Kampel, G. Assumpção, et al., "Optical Probing of Mechanical Loss of a Si_3N_4 membrane below 100 mK," preprint, arXiv, arXiv:1611.00878, (2016).

38. F. Zhou, Y. Bao, J. J. Gorman, and J. R. Lawall, "Cavity Optomechanical Bistability With an Ultrahigh Reflectivity Photonic Crystal Membrane," *Laser & Photonics Reviews* 17, no. 10 (2023): 2300008.

39. F. Zhou, Y. Bao, J. Gorman, and J. R. Lawall, "Ultrahigh Reflectivity Photonic Crystal Membranes With Optimal Geometry," *APL Photonics* 9, no. 7 (2024): 076120.

40. M. H. de Jong, J. Li, C. Gärtner, R. A. Norte, and S. Gröblacher, "Coherent Mechanical Noise Cancellation and Cooperativity Competition in Optomechanical Arrays," *Optica* 9, no. 2 (2022): 170–176.

41. G. Enzian, Z. Wang, A. Simonsen, et al., "Phononically Shielded Photonic-Crystal Mirror Membranes for Cavity Quantum Optomechanics," *Optics Express* 31, no. 8 (2023): 13040–13052.

42. X. Chen, C. Chardin, K. Makles, et al., "High-Finesse Fabry–Perot Cavities With Bidimensional Si_3N_4 Photonic-Crystal Slabs," *Light: Science & Applications* 6, no. 1 (2017): e16190.

43. V. Dumont, S. Bernard, C. Reinhardt, A. Kato, M. Ruf, and J. C. Sankey, "Flexure-Tuned Membrane-at-the-Edge Optomechanical System," *Optics Express* 27, no. 18 (2019): 25731–25748.

44. C. H. Bui, J. Zheng, S. Hoch, L. Y. Lee, J. Harris, and C. Wei Wong, "High-Reflectivity, High-Q Micromechanical Membranes via Guided Resonances for Enhanced Optomechanical Coupling," *Applied Physics Letters* 100, no. 2 (2012): 021110.

45. T. Mitra, G. Singh, A. A. Darki, S. P. Madsen, and A. Dantan, "Narrow-Linewidth Fano Microcavities With Resonant Subwavelength Grating Mirror," *Optics Express* 32, no. 9 (2024): 15667–15679.

46. M. Karuza, C. Biancofiore, M. Bawaj, et al., "Optomechanically Induced Transparency in a Membrane-in-the-Middle Setup at Room Temperature," *Physical Review A–Atomic, Molecular, and Optical Physics* 88, no. 1 (2013): 013804.

47. A. D. Hyatt, O. A. Flores, A. R. Agrawal, C. A. Condos, and D. J. Wilson, "Fabrication and Characterization of High-Q Silicon Nitride Membrane Resonators," *Journal of Visualized Experiments (JoVE)* no. 222 (2025): e68706.

48. S. Kini Manjeshwar, A. Ciers, J. Monsel, et al., "Integrated Microcavity Optomechanics With a Suspended Photonic Crystal Mirror Above a Distributed Bragg Reflector," *Optics Express* 31, no. 19 (2023): 30212–30226.

49. G. J. Hornig, S. Al-Sumaidae, J. Maldaner, L. Bu, and R. DeCorby, "Monolithically Integrated Membrane-in-the-Middle Cavity Optomechanical Systems," *Optics Express* 28, no. 19 (2020): 28113–28125.

50. L. Norder, S. Yin, M. H. de Jong, et al., "Pentagonal Photonic Crystal Mirrors: Scalable Lightsails With Enhanced Acceleration via Neural Topology Optimization," *Nature Communications* 16, no. 1 (2025): 2753.

51. J. Guo, R. Norte, and S. Gröblacher, "Feedback Cooling of a Room Temperature Mechanical Oscillator Close to Its Motional Ground State," *Physical Review Letters* 123, no. 22 (2019): 223602.

52. M. Xu, R. J. Elbertse, A. Keşkekler, et al., "Measuring Casimir Force Across a Superconducting Transition," preprint, arXiv, arXiv:2504.10579, (2025).

53. M. H. de Jong, M. A. ten Wolde, A. Cupertino, S. Gröblacher, P. G. Steeneken, and R. A. Norte, "Mechanical Dissipation by Substrate–Mode Coupling in Sin Resonators," *Applied Physics Letters* 121, no. 3 (2022): 032201.

21951071, 0, Downloaded from https://advanced.onlinelibrary.wiley.com/doi/10.1002/adom.71871, Wiley Online Library on [22/10/2026]. See the Terms and Conditions (https://onlinelibrary.wiley.com/terms-and-conditions) on Wiley Online Library for rules of use; OA articles are governed by the applicable Creative Commons License

54. D. J. Wilson, *Cavity Optomechanics With High-Stress Silicon Nitride Films* (California Institute of Technology, 2012).

55. J. P. Moura, R. A. Norte, J. Guo, C. Schäfermeier, and S. Gröblacher, "Centimeter-Scale Suspended Photonic Crystal Mirrors," *Optics Express* 26, no. 2 (2018): 1895–1909.

56. A. Agrawal, J. Manley, D. Allepuz-Requena, and D. Wilson, "Focusing Membrane Metamirrors for Integrated Cavity Optomechanics," *Optica* 11, no. 9 (2024): 1235–1241.

57. J. Guo, R. A. Norte, and S. Gröblacher, "Integrated Optical Force Sensors Using Focusing Photonic Crystal Arrays," *Optics express* 25, no. 8 (2017): 9196–9203.

Supporting Information

Additional supporting information can be found online in the Supporting Information section.

Supporting File: adom71871-sup-0001-SuppMat.pdf.

21951071, 0, Downloaded from https://advanced.onlinelibrary.wiley.com/doi/10.1002/adom.71871, Wiley Online Library on [22/10/2026]. See the Terms and Conditions (https://onlinelibrary.wiley.com/terms-and-conditions) on Wiley Online Library for rules of use; OA articles are governed by the applicable Creative Commons License